Laser spectroscopy measurement of the 2s-hyperfinesplitting in lithium-like bismuth

Sánchez, R.; Lochmann, M.; Jöhren, R.; Andelkovic, Z.; Anielski, D.; Botermann, B.;
Bussmann, M.; Dax, A.; Frömmgen, N.; Geppert, C.; Hammen, M.; Hannen, V.; Kuehl, T.;
Litvinov, Y.; Coto, R. L.; Stoehlker, T.; Thompson, R.; Vollbrecht, J.; Wen, W.;
Weinheimer, C.; Will, E.; Winters, D.; Noertershaeuser, W.;

Laser spectroscopy measurement of the 2s-hyperfine splitting in lithium-like bismuth

Rodolfo Sánchez[1], Matthias Lochmann[1,2,3], Raphael Jöhren[4], Zoran Andelkovic[1], Denis Anielski[4], Benjamin Botermann[1,3], Michael Bussmann[5], Andreas Dax[6] ‡, Nadja Frömmgen[3], Christopher Geppert [2,3], Michael Hammen[2], Volker Hannen[4], Thomas Kühl[1,7], Yuri A. Litvinov[1], Rubén López-Coto[4] §, Thomas Stöhlker[1,7], Richard C. Thompson[8], Jonas Vollbrecht[4], Weiqiang Wen[9], Christian Weinheimer [4], Elisa Will[3], Danyal Winters[1] and Wilfried Nörtershäuser[2,3]

[1] GSI Helmholtzzentrum für Schwerionenforschung GmbH, 64291 Darmstadt, Germany.

[2] Institut für Kernphysik, Technische Universität Darmstadt, 64289 Darmstadt, Germany.

[3] Institut für Kernchemie, Johannes Gutenberg-Universität Mainz, 55128 Mainz, Germany.

[4] Institut für Kernphysik, Westfälische Wilhelms-Universität Münster, 48149 Münster, Germany.

[5] Helmholtz-Zentrum Dresden-Rossendorf, 01314 Dresden, Germany.

[6] Department of Physics, University of Tokyo, Japan.

[7] Helmholtz-Institut Jena, 07743 Jena, Germany.

[8] Department of Physics, Imperial College London, London SW7 2AZ, United Kingdom.

[9] Institute of Modern Physics, Lanzhou 730000, China.

E-mail: `r.sanchez@gsi.de`

Abstract. The $2s$ hyperfine splitting in lithium-like bismuth $^{209}\text{Bi}^{80+}$ and the $1s$ splitting in hydrogen-like bismuth $^{209}\text{Bi}^{82+}$ were measured using laser spectroscopy at the experimental storage ring ESR. The specific difference between these experimental values has been suggested by theory as an appropriate observable for tests of strong-field bound-state QED, since uncertainties introduced by the nuclear magnetic moment distribution (Bohr-Weisskopf effect) should be largely cancelled. The electrons in these heavy highly charged ions experience one of the strongest static magnetic fields available in the laboratory and are thus probes to test QED in a magnetic-field regime that was not accessible previously. Here we present the laser spectroscopic method in detail, discuss all improvements that finally led to the first laser fluorescence detection of the lithium-like ion and evaluate all statistical and systematic uncertainties in the measurements. Our result provides the first significant test of the validity of the specific-difference approach with an accuracy of about 1%. Conclusions for further measurements are discussed.

‡ Present address Paul Scherrer Institut, 5232 Villingen, Switzerland.

§ Present address Max-Planck-Institut für Kernphysik, 69029 Heidelberg, Germany

PACS numbers: 32.10.Fn, 31.30.J-

1. Introduction

The fundamental theory of the interaction between light and matter, also known as quantum electrodynamics (QED), is about to celebrate its 70 years of success in modern physics. Throughout these seven decades QED has conquered all tests and therefore it is considered as the most precisely tested theory in physics. Impressive examples of these tests include the high accuracy measurements of the electron g-factor [1], the Lamb-Shift in hydrogen [2], the recent g_J-factor measurements in hydrogen-like Si^{13+} [3] and the "isotope shift" of the electron bound state g-factor in ^{40,48}Ca [4]. Measurements with moderate accuracy are presently also available in highly charged heavy systems, like for example x-ray spectroscopy on hydrogen-like U^{91+} [5] and lithium-like U^{89+} [6]. With the exception of the proton radius puzzle [7, 8], where the origin of the discrepancy with other experiments is still unclear, one can clearly state that QED is so far in accordance with all experimental results. However QED-tests in the regime of extreme magnetic fields, which are as large as 10^{10} T on the surface of heavy atomic nuclei and on neutron stars, were missing up to now. These are complementary to all other tests and can be accessed via measurements of the hyperfine splitting (HFS) and the g_J-factors from s-electrons in highly charged heavy ions. The hyperfine splitting operator shows a characteristic radial dependence of $1/\langle r^{-2} \rangle$, leading to average magnetic fields of 10 000 T for an electron in the $1s$ orbital, whereas the g_J-factor has a radial dependence of $\langle r \rangle$. Therefore the hyperfine splitting is considerably more sensitive to the strong magnetic fields close to the nucleus [9]. Measurements of the $1s$ hyperfine splitting in several hydrogen-like heavy ions were carried out mainly in the nineties reaching a relative accuracy at the level of 10^{-4}. Hydrogen-like bismuth and lead were measured by laser spectroscopy at the experimental storage ring ESR [10, 11] while holmium, rhenium and thallium by passive emission spectroscopy in an electron beam ion trap (EBIT) at LLNL [12, 13, 14]. However, the theoretical calculations of the hyperfine splitting in these systems appeared to be dominated by the uncertainty of the extension of the nuclear magnetization distribution (Bohr-Weisskopf effect). This uncertainty is almost as large as the total QED contribution and therefore a high precision test of the QED effects using the hyperfine splitting of these highly charged ions was up to now not possible. Instead it was suggested by Shabaev et al. [15] to determine a "specific difference" between the hyperfine splittings in hydrogen-like and lithium-like ions, chosen in a way to be largely independent of all nuclear structure effects, particularly from the Bohr-Weisskopf effect. Unfortunately, most of the one-electron QED contributions cancel in this difference as well. The dominating QED contribution in the specific difference is the so-called screened QED, arising in the electron-electron interaction in the lithium-like system. To become sensitive to the remaining one-electron QED and test it on a level of a few %, requires both hyperfine splittings to be measured with a relative accuracy of better than 10^{-6}. The isotope ^{209}Bi is one of the best candidates to test this new approach because both hyperfine splittings are in a wavelength regime accessible for laser spectroscopy. The hyperfine splitting in hydrogen-like bismuth was measured at

the ESR in 1994, performing laser spectroscopy on an ion beam moving at 58.7 % of the speed of light [10]. However in the case of lithium-like bismuth only one measurement was reported so far with a relative accuracy of 3% [16] performed with x-ray classical emission spectroscopy in an EBIT. At least three attempts to observe this transition by direct laser spectroscopy at the ESR failed since 1998 even though the resonance was searched for at the predicted values as well as within a large wavelength range on both sides. This triggered many speculations including even doubts in the calculations of the hyperfine splitting as well as doubts of QED calculations in the presence of strong magnetic fields. In this respect there was a great demand to measure this transition with a better accuracy than reported in [16]. With an improved technique, we were finally able to observe this transition by direct laser spectroscopy in 2011 at the ESR [17] and to clarify why it was not found in previous attempts. Here we present the advances in the experimental technique that led to the first direct obeservation, discuss all systematic uncertainties, their influence on the specific difference and the conclusions that can be drawn from the results.

2. Hyperfine Splitting

For atoms with non-vanishing nuclear spin the fine structure lines split due to the magnetic dipole interaction of the nuclear magnetic moment $\mu_I = g_I\mu_N\mathbf{I}$ with the magnetic field created by the electrons at the nucleus $B_e = B_0\mathbf{J}$. Here g_I is the nuclear g-factor, μ_N the nuclear magneton, $\mathbf{I}$ the nuclear spin and $\mathbf{J}$ the total angular momentum of the electrons. This interaction shifts the level energies dependent on the total angular momentum $\mathbf{F} = \mathbf{I} + \mathbf{J}$. While the splitting in hydrogen is only about 1420 MHz between the $F = 0, 1$ hyperfine levels, the corresponding splitting in hydrogen-like ions increases with Z^3. At the same time, the lifetime of the upper hfs state decreases with Z^{-9} from 11 Ma for the $F = 1$ state in hydrogen to 397 μs for the $F = 5$ state in hydrogen-like bismuth. Therefore some nuclei with $Z \geq 70$ exhibit a hyperfine transition in the optical regime and the lifetime becomes short enough to render laser spectroscopy possible even though at extremely low scattering rates.

2.1. Hydrogen-like bismuth

Hydrogen-like ^{209}Bi^{82+} exhibits the largest ground-state hyperfine splitting of all stable isotopes. The M1 transition between the two hyperfine states was measured by collinear laser spectroscopy at the ESR [10] in 1994, providing

$$\lambda^{(1s)} = 243.87(4) \text{ nm} \quad \text{corresponding to} \quad \Delta E^{(1s)} = 5084.1(8) \text{ meV}. \quad (1)$$

Individual contributions to this splitting as presented in [18] are summarized in table 1. Relativistic effects are dominant, and the finite nuclear size correction of the charge distribution contributes on the 10 % level. The Bohr-Weisskopf correction is only on the 1 % level but its relative uncertainty is almost 50 % and therefore of similar size to

Table 1. Contributions to the hyperfine splitting in hydrogen-like bismuth. Values taken from [18]

Contribution	Size [meV]
Fermi value (non relativistic)	2747.9(1)
Relativistic value	5839.3(3)
Corrections	
Nuclear charge distribution	−648.2(7)
Bohr-Weisskopf effect	−61(27)
One-electron QED	−29.8
Total	5100(27)

the complete one-electron QED contribution. The reported measurement of this HFS splitting [10] is about 30 times more accurate than theory predictions.

Other hydrogen-like ions having the $1s$ hyperfine splitting in the visible regime, were also addressed experimentally. Figure 1 shows the results. One can clearly see a disagreement between theory and experiment as large as 30 meV. Only for ^{207}Pb do experiment and theory agree, provided that the magnetic moment measured by nuclear magnetic resonance is employed for the calculation, while it disagrees if the nuclear magnetic moment measured by optical pumping is used. The discrepancy between the theoretical and experimental results is attributed to the Bohr-Weisskopf effect, which depends strongly on the nuclear model employed to describe the nuclear magnetization distribution. The open blue circles and open black squares are results of calculations using a single-particle nuclear model [18, 19] which works better for nuclei close to shell closures. The open green triangles show results using a dynamic correlation nuclear model [20]: in some cases the results are closer to the experiment but in general also the model differs significantly from experiment.

2.2. Specific difference and lithium-like bismuth

An alternative method was developed towards the end of the 1990's by Shabaev and coworkers [15]. It is based on the fact that the ratio of the Bohr-Weisskopf correction in the $2s$ hyperfine splitting in lithium-like ions to the Bohr-Weisskopf correction in the $1s$ hyperfine splitting in hydrogen-like ions can be calculated with high accuracy because it is mainly a function of the atomic structure [21] while nuclear corrections are largely canceled if the ratio of the electron probability density inside the nuclear volume is taken into account. This method was further developed and finally proposed in [15], where the specific difference between the hyperfine splitting in hydrogen-like, $\Delta E^{(1s)}$, and lithium-like, $\Delta E^{(2s)}$, bismuth is defined as:

$$\Delta' E = \Delta E^{(2s)} - \xi \Delta E^{(1s)}. \tag{2}$$

Here the isotope-dependent parameter ξ is chosen to make the specific difference independent of the nuclear structure effects, particularly independent from the Bohr-
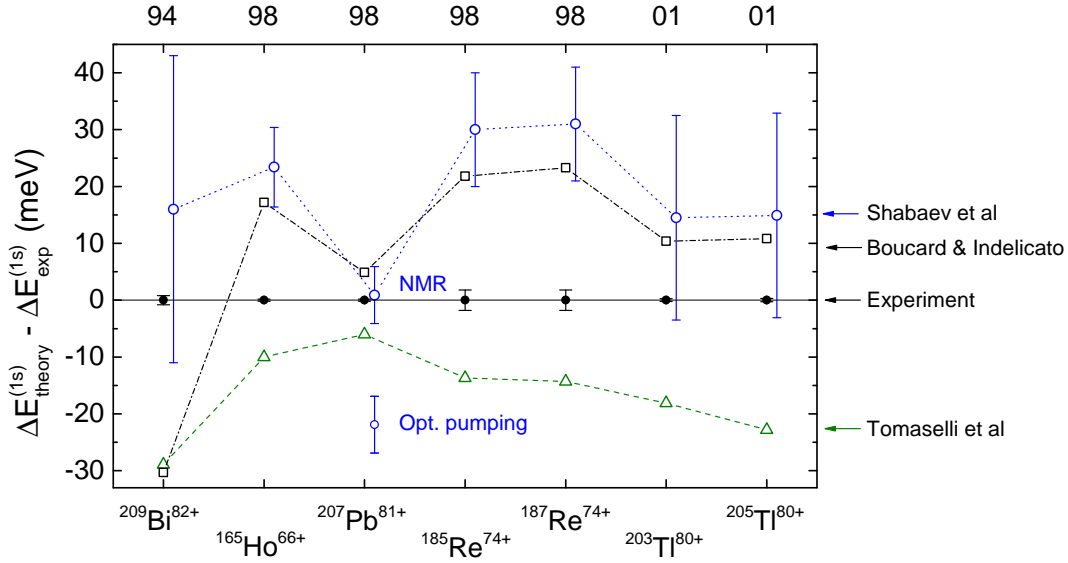
Figure 1. Comparison between the experimental and theoretical values in the hyperfine splitting for different hydrogen-like ions. The data are shown as a function of the experimental publication date. The experimental values define the zero reference line. The open blue circles, green triangles and black squares are the calculations from Shabaev and Tomaselli and Boucard, respectively. For lead, the theoretical prediction of Shabaev *et al* is given for the two inconsistent nuclear magnetic moments given in the literature. The values are taken from [18, 19, 20].

Weisskopf contribution. Hence $\Delta'E$ can then be calculated with high accuracy. For ^{209}Bi, $\xi = 0.16886$.

The advantage of this approach is two-fold.

- It allows the value for $\Delta E^{(2s)}$ to be predicted based on the measured $\Delta E^{(1s)}$ value because the specific difference can be calculated with high accuracy and therefore the uncertainty of the predicted $\Delta E^{(2s)}$ value is completely dominated by the experimental uncertainty of $\Delta E^{(1s)}$. In table 2 the predicted values for the hyperfine splitting in lithium-like bismuth are given as a function of the year. The values listed as "Theory + Exp." were obtained using the specific difference approach.

- After $\Delta E^{(2s)}$ is experimentally determined, then it can be used together with the $\Delta E^{(1s)}$ experimental value to test the QED contributions present in the specific difference. Table 3 summarizes the different contributions to $\Delta'E$ for ^{209}Bi. Unfortunately one-electron QED is mostly canceled and $\Delta'E$ is dominated by the interelectronic interaction in $\Delta E^{(2s)}$ which is completely absent in $\Delta E^{(1s)}$. The uncertainties of the total value in the theoretical description originate from the screened QED contributions and in order to test them, both hyperfine transitions have to be measured with an accuracy at the 10^{-6} level according to [22].

Three attempts to observe the $2s$ hyperfine transition in lithium-like bismuth by direct laser spectroscopy at the ESR failed between 1998 and 2004 even though the

Table 2. Theoretical predictions of $\Delta E^{(2s)}$ based on pure theory or on a combination of theoretical calculations and the hyperfine splitting in hydrogen-like bismuth $\Delta E^{(1s)}$ (Theory + Exp.).

Year	$\Delta E^{(2s)}$ [meV]	$\lambda^{(2s)}$ [nm]	Method	Reference
1998	800(4)	1550(8)	Theory	[21]
1998	796.9(2)	1555.8(4)	Theory + Exp.	[23]
2000	783.9(3.0)	1582(6)	Theory	[24]
2000	792.8	1563.9	Theory	[19]
2000	797.1(2)	1555.44(39)	Theory + Exp.	[25]
2001	797.15(13)	1555.34(25)	Theory + Exp.	[26]
2001	797.18(14)	1555.28(27)	Theory + Exp.	[15]
2012	797.16(14)	1555.32(27)	Theory + Exp.	[22]

Table 3. Individual contributions to $\Delta'E$ in meV for ^{209}Bi. Values are taken from [22]. The first uncertainty originates from the calculations while the second one comes from nuclear effects, which do not completely cancel in the specific difference.

Effect	$\Delta E^{(2s)}$	$\xi\Delta E^{(1s)}$	$\Delta'E$
Dirac value	844.829	876.638	−31.809
QED	−5.052	−5.088	0.036
Interel. interaction $\sim 1/Z$	−29.995		−29.995
Interel. interaction $\sim 1/Z^2$	0.258		0.258
Interel. interaction $\sim 1/Z^3$	−0.003(3)		−0.003(3)
Screened QED	0.193(2)		0.193(2)
Total			−61.320(4)(5)

transition was searched many times at the predicted values listed in table 2. The experiment is more challenging than the search for the hydrogen-like transition since the transition rate between the $2s$ levels is only

$$w = 1/\tau = 12.2(2) \text{ s}^{-1}, \tag{3}$$

and therefore two orders of magnitude smaller than the one in hydrogen-like bismuth [21]. Moreover, the transition wavelength is in the infrared region and the photon detection is considerably less efficient and is disturbed by higher noise levels. The only experimental value reported so far for $\Delta E^{(2s)} = 820(26)$ meV was indirectly obtained in a SuperEBIT [16], deduced from the hyperfine splitting in the $2s_{1/2} - 2p_{1/2}$ x-ray transition. The uncertainty is as large as the interelectronic interaction energy and more than five times larger than the QED contribution and therefore it can not be used to test the contributions in specific difference.

3. Experimental Setup

3.1. Overview

Figure 2 shows a schematic view of the experimental storage ring [27], with the main components for laser spectroscopy of the $1s\,^2\mathrm{S}_{1/2}(F=4) \to 1s\,^2\mathrm{S}_{1/2}(F=5)$ hyperfine transition in hydrogen-like bismuth and $2s\,^2\mathrm{S}_{1/2}(F=4) \to 2s\,^2\mathrm{S}_{1/2}(F=5)$ hyperfine transition in lithium-like bismuth, respectively. The ions are produced at the GSI accelerator facility and either hydrogen-like or lithium-like bismuth ions are stored at the ESR at an energy of 400 MeV/u, corresponding to an ion velocity of 71% of the speed of light. The momentum distribution of the injected ions is reduced by electron cooling and two bunches of ions are produced by applying the second harmonic of the free revolution frequency to one of the two radiofrequency cavities installed in the ring. One of the two bunches interacts repeatedly with the laser pulses which are produced by a dye laser, while the second one is used as reference for background correction. Due to the relativistic Doppler shift both hyperfine transitions of the ions are shifted to the visible regime in the laboratory frame. Because both hyperfine transitions are rather long lived, the fluorescence takes place along the complete ring circumference. Therefore it can be monitored at the optical detection section located on the opposite side of the ESR from the electron cooler, while the laser beam is superimposed with the ion beam at the electron-cooler section. This protects the photomultipliers (PMT) from the stray light produced by the laser pulse. In the laboratory frame the emitted fluorescence is neither isotropic nor monochromatic, therefore mirror systems with optimized geometries are installed inside the vacuum beamline to reflect the fluorescence photons towards PMTs located outside the vacuum beamline. The PMT-signals are amplified, guided outside the ESR cave and discriminated for data recording and analysis. Resonances are obtained by recording the PMT signal as a function of the laser wavelength. In the following sections the individual parts of the experimental setup are described in more detail.

3.2. Production of the H- and Li-like bismuth

Multiply charged (Bi^{4+}) ions were produced using a metal vapor vacuum arc (MEVVA) ion source [28] and afterwards accelerated by the linear accelerator UNILAC‖ before they were transferred to the synchrotron SIS-18¶, where they were further accelerated to an energy of nearly 400 MeV/u. After extraction they passed a thin stripping foil. For the production of hydrogen-like bismuth, a copper foil with an area density of 40 mg/cm^2, while for the production of lithium-like bismuth a carbon foil with an area density of 29 mg/cm^2, were used.


‖ UNILAC: Universal linear accelerator.
¶ SIS: Schwerionensynchrotron (heavy-ion-synchrotron) with a magnetic rigidity of 18 Tm.

3.3. Experimental Storage Ring - ESR

The ions were then injected into the ESR at about 400 MeV/u corresponding to an ion velocity of $\beta \approx 0.71$. The ESR is shown in figure 2: The ion orbit is closed by six 60° dipole magnets while the quadrupoles are used for focusing and sextupole magnets are used to perform higher order ion optical corrections [27]. The ring is designed to have an ion-beam orbit of about 108.36 m, but the real value can vary up to 100 mm according, for example, to the ion-optic settings, the ion-charge state and the ion-beam energy. In our case the corresponding ion-revolution frequency was of the order of 2 MHz and it was measured with a 10^{-6} accuracy using a broadband Schottky spectrometer [29]. Typical ion beam currents in the ring were between 2 and 3 mA, corresponding to about 10^8 stored ions. In the electron cooler the stored ions are superimposed with an electron beam of about 50 mm diameter. To match the ion velocity the electron cooler was operated at -214 kV, the maximum value where it can be operated under stable conditions for extended periods of time. The length of the electron-ion interaction region is about 2 m. In this way the ions are cooled down over several seconds with "cold" electrons. The hot electron beam is collected again on the HV-platform after the interaction. Electron-cooling reduces the longitudinal momentum spread of the ions [30] and therefore the resonance linewidth in the laboratory frame. This leads to a more efficient excitation and a reduction of the ion beam diameter.

As shown in figure 2, the ring has two straight sections which extend outside the dipole magnets. These vacuum tubes end in axial windows for optical access. Laser beams can be coupled either in a co-propagating (collinear) or counter-propagating (anticollinear) configuration with respect to the ion beam direction. For this experiment, the laser-ion interaction region was located at the electron-cooler side of the ring. Utilizing the Doppler shift $\lambda_{\mathrm{L}} = \lambda_0 \gamma (1 - \beta \cos \theta)$ in the collinear ($\theta = 0°$) and anticollinear ($\theta = 180°$) configuration the transition frequencies are shifted in the laboratory frame from 1555 nm to 640 nm (lithium-like, collinear) and from 243 nm to 590 nm (hydrogen-like, anticollinear). Hence, both hyperfine transitions can be addressed with one laser system, as described in section 3.4. In order to increase the excitation efficiency and to reduce the background level, the ions were collected in two bunches revolving in the ESR with a phase shift of 180°. To this aim the second harmonic of the revolution frequency is applied to one of the two RF cavities in the ring. The length of the ion bunch is approximately 10–12 m [32, 33]. One bunch is repeatedly irradiated at a repetition rate of 30 Hz by the laser along the electron cooler section, while the second bunch (reference bunch) is located at the opposite side of the ring at the optical detection region. Photons observed when the reference bunch is passing the detection region originated from collisional excitation of residual gas atoms. It can be utilized to detect the arrival of a bunch at this region as discussed below. Half a revolution period later (~ 250 ns) the excited bunch passes the optical detection region while the reference bunch is at the electron cooler. Even for hydrogen-like bismuth with a half-life on the order of 560 μs in the laboratory frame [34] the fluorescence lasts for
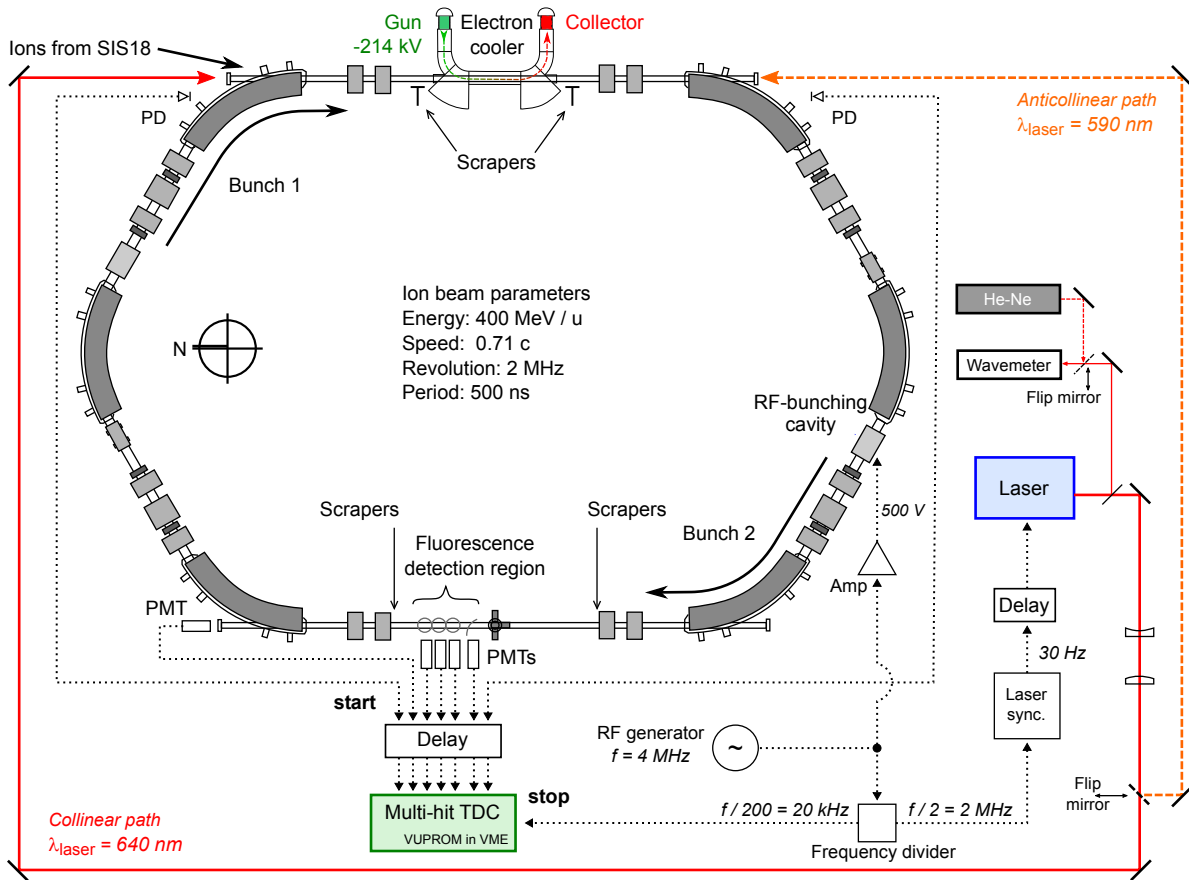
Figure 2. Schematic view of the ESR and the experimental setup including the laser and data acquisition system. Laser beam paths are shown as solid and dashed lines while electrical signals are represented by dotted lines. A detailed description of the setup is given in the text.

more than 1000 revolutions and the fluorescence photons have to be collected all the time with respect to the signal bunch position as discussed below.

3.4. Laser system

M1 transitions with lifetime in the ms regime have a linewidth of only 100 Hz. This combined with the large Doppler broadening requires a laser with a large bandwidth and high pulse-power in order to efficiently excite a large fraction of the revolving ions. The light for both transitions was produced by a pulsed dye laser (*Sirah*, Cobra Stretch G-1800) pumped with up to 600 mJ of the second harmonic of a Nd:YAG laser (*Spectra Physics*, Quanta Ray Pro 290-30).

3.4.1. Dye laser The dye laser was used in the Litrow configuration with a grating of 1800 lines/mm. The laser is equipped with two cells, one rectangular cell used for both the oscillator and the preamplifier and one cylindrical cell for the main amplifier. The pumping laser beam is split into three components with two beam splitters distributing

the laser power over the three spots in the two cells in a proportion of roughly 5:15:80 for the oscillator, preamplifier and main amplifier, respectively.

The oscillator consists of a high reflecting mirror used as output coupler, the grating and a prism beam expander which was customized for this experiment. The laser can be operated such that either only a part of the complete grating-length or the complete grating-length is illuminated. Hence the laser can be switched between a broadband mode with a linewidth of about 2.0 cm^{-1} (≈ 60 GHz) used during the search-mode, and a narrow-band mode with a width of 0.64 cm^{-1} when performing the spectroscopy after the resonance had been observed.

Sulforhodamin B dissolved in ethanol at a concentration of 0.2 g/l was used in the oscillator and preamplifier cell when operated for hydrogen-like bismuth. The tuning range of this dye is 585 nm - 600 nm with peak energy at 591 nm. The dye concentration for the main amplifier is 1/8 of the oscillator in order not to damage the glass of the dye cell. We typically obtained 120 mJ output energy. For lithium-like bismuth 0.3 g/l DCM dissolved in a solution of 50% Ethanol and 50% DMSO was used in the oscillator and preamplifier cell. Here the dye concentration for the main amplifier is also 1/8 of the oscillator. The wavelength tuning range is 615 nm - 670 nm with the maximum at 639 nm. An output energy of 150 mJ was achieved.

3.4.2. Wavelength determination The wavelength of the laser was monitored using a wavemeter of the Fizeau interferometer type (*ATOS*, LM007). For this purpose the laser beam was split and a small fraction of the beam was coupled into an optical fiber which is fed into the wavemeter. Inside the wavemeter the light is split four times and directed to four temperature stabilized interferometers of different thickness. Depending on the laser linewidth, the wavemeter can be operated with different numbers of interferometers. In our case only one interferometer could be used when the laser was operated in broadband configuration while two interferometers were used in narrowband configuration. The device has a USB interface to exchange commands and measure data. The wavemeter can be triggered either internally or externally by using the external input trigger. In order to calibrate the wavemeter a stabilized and calibrated He:Ne laser was also coupled into the wavemeter using a flipable mirror. The calibration was performed regularly during the beamtime. The influence of the reduced number of interferometers on the accuracy of the wavelength measurement was investigated after the beamtime and the shift by an asymmetric spectral lineshape was conservatively estimated leading to total systematic uncertainties for the laboratory wavelength of $\Delta\lambda_{\mathrm{ATOS,BB}} = 200$ pm and $\Delta\lambda_{\mathrm{ATOS,NB}} = 15$ pm for broadband and narrowband operation, respectively.

3.4.3. Laser beam transport The laser laboratory is located outside the ESR cave and the laser beam has to be transported by means of high-reflective mirrors to the interaction region at the electron cooler as shown in figure 2. The mirrors have a diameter of 75 mm and a high-reflection coating at 45° for 600 nm - 650 nm. The distance between the laser and the interaction region is 50 m and 80 m for anticollinear

and collinear excitation, respectively. A telescope was set up on the laser table at a distance of 1 m from the laser output to enlarge the beam for transport and create a weak focus inside the electron cooler section. The telescope consisted of a plano-concave lens with a focal length of $f = -400$ mm and a plano-convex lens with $f = +800$ mm. The distance between both lenses was set to about 400 mm and a motorized linear stage on which the plano-convex lens was mounted, allowed fine tuning of the distance until a spot of about 15 mm FWHM was obtained at the electron cooler position. In order to change from the anticollinear to the collinear configuration a flip mirror was used as it is schematically shown in figure 2. Inside the ESR-Cave the laser path and optics for steering the beam are isolated by protective pipes and cages, respectively. Inside the last cage a periscope is located which allows the alignment of the laser beam in the electron cooler section. Overlap between ion beam and laser beam was ensured using two beam scrapers (T-form) which are located symmetrically with respect to the electron-cooler center position. Once the ion beam path was optimized inside the ring and its position at the electron cooler was determined with the help of the scrapers, the ion beam was turned off and the laser beam was adjusted relative to the scraper positions.

3.4.4. Position stabilization Since the laser-beam has to be transported over long distances, its position and pointing is easily affected by small disturbances in the experimental area cage's air. To counteract those and to ensure pointing stability at the interaction region, we used a commercial active laser-beam stabilization system (*TEM*, Aligna). For this purpose, a small fraction of the laser beam was splitted into two beams by using a wedge plate in front of the entrance viewport of the ESR. One of these beams was used for monitoring the beam spot at the electron cooler while the second one was used for the active laser-beam stabilization.

3.5. Fluorescence Detection

Due to the long lifetime of the transition compared to the ion revolution time in the ring ($\tau \gg t_{\mathrm{Rev}}$), fluorescence detection can be performed on the opposite side of the ring and therefore completely free of the scattered laser light.

3.5.1. Spectral emission and spatial properties of fluorescence of relativistic ions At relativistic velocities the isotropic emission in the ion rest frame is transformed into an emission cone in the forward direction due to the relativistic aberration. The flux ϕ in direction θ in the laboratory frame is changed by a factor D^3.

$$\frac{\phi_0(\theta_0)}{\phi(\theta)} = D^3 = \left(\frac{\lambda}{\lambda_0}\right)^3, \tag{4}$$

where the index 0 denotes the rest frame of the ion and D is given by

$$D = \frac{1}{\gamma(1 - \beta\cos\theta)}, \tag{5}$$

where θ is the observation angle with respect to the ion velocity. At a velocity of 71% of c this increases the flux in the forward direction by a factor of 5.9, and reduces it by 50% and 17% in perpendicular and backward directions, respectively. Additionally, the photon wavelength changes as a function of the emission angle in the laboratory frame according to $\lambda = D\lambda_0$. In figure 3 a two-dimensional projection of the fluorescence in the laboratory frame is shown. The length of the arrow indicates the emission probability and the color code indicates the wavelength. For hydrogen-like ions this leads to a variation from 591 nm (laser wavelength) to 100 nm from backward to forward angles. Taking the transmission of the quartz window and the sensitivity of the solar blind PMT into account, all photons emitted between about 54° ($\lambda > 200$ nm) and 79° ($\lambda < 370$ nm) in the forward direction are detectable. Detection of the fluorescence emitted by the lithium-like bismuth ions in the ring is considerably more challenging. Due to the longer lifetime of the upper hyperfine level of $\tau \approx 82$ ms [21], the corresponding fluorescence rate is more than two orders of magnitude smaller than for hydrogen-like bismuth. Moreover, the infrared transition wavelength in the rest frame is shifted to 3.77 μm in backward and 641 nm (laser wavelength) in forward direction. The sensitivity of the PMT tube restricts the detection of photons to wavelengths of $641 \leq \lambda \leq 790$ nm and corresponding emission angles between $0 \leq \theta \leq 25°$.

3.5.2. Segmented mirror system Most of the laser experiments carried out at ESR until 2010 have used a segmented mirror system. The mirror was originally designed and successfully applied to collect the fluorescence from the hyperfine transition in hydrogen-like lead in 1997 [11] and of hydrogen-like bismuth during the later trials to find the transition in lithium-like bismuth. A schematic drawing is shown on the left of figure 3. It consists of 11 segmented aluminum sheets. The foils are geometrically arranged to allow the reflection of the fluorescence photons emitted between 20° and 60° with respect to the ion beam direction of motion. The lower part is folded in an elliptical shape. The parameters of the ellipsoid are chosen to have one focal point at the ion-beam path while the other one is located at the detector's surface located about 50 mm away from the ion beam axis. The upper part is spherically shaped, so the fluorescence hitting this part of the mirror is reflected first to the elliptical part and from there to the detector. The sheets are additionally tilted by about 15° in order to reflect the fluorescence emitted into forward directions more efficiently; this additional tilting does not modify the ellipse shape significantly. The sheets are mounted in an aluminum frame and the complete system is installed in a vacuum chamber CF NW250 with a length of about 1 m. Three clear hole flanges CF NW100 are available to install windows for optical access.

For hydrogen-like bismuth, a "solar blind" PMT (*Thorn EMI*, 9422A) was installed at the first window from the ion beam direction (see figure 3). The optical viewport is made of quartz glass; the PMT's cathode is sensitive in the wavelength regime from 120 nm to 350 nm. The fluorescence signal from hydrogen-like bismuth was however up to 50 times smaller compared to the fluorescence signal recorded in previous beamtimes
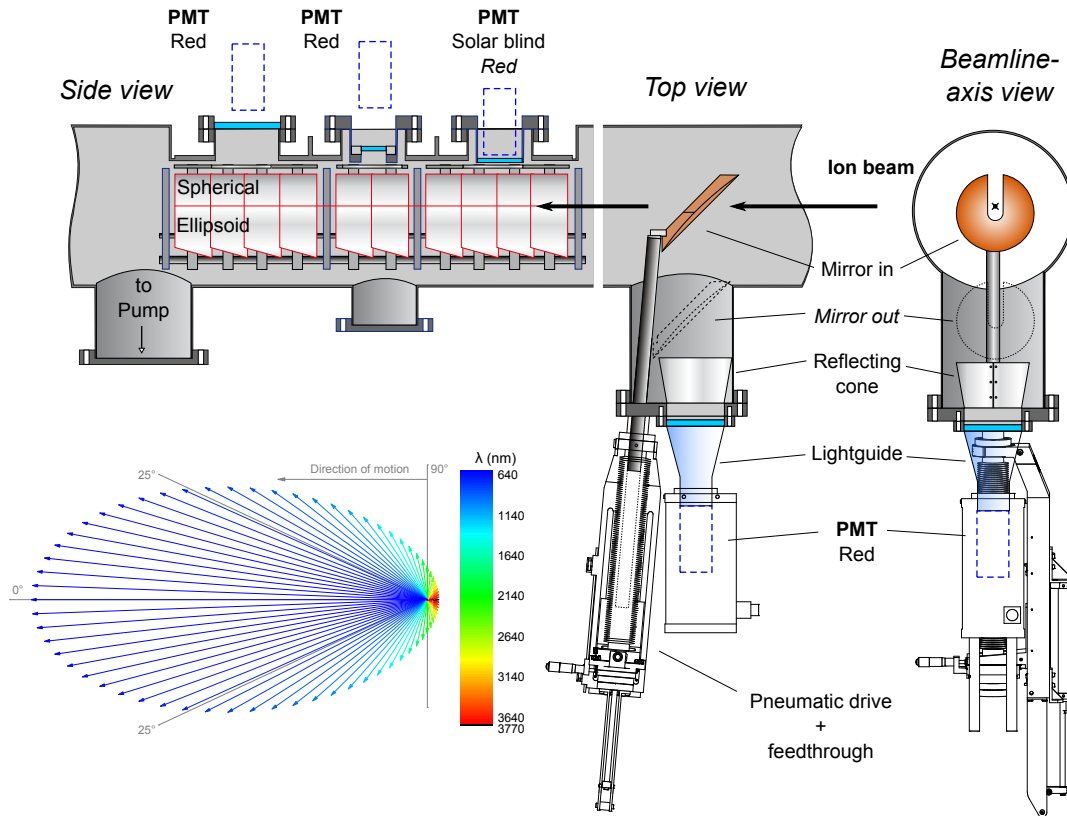
Figure 3. Schematic view of the mirror system for fluorescence detection at the ESR. A two-dimentional projection of the fluorescence emitted by the ion moving with $\beta = 0.71$ is shown in the bottom left-hand side.

even though we noticed that the background was comparable.

In the case of lithium-like bismuth on all three windows PMTs (*Hamamatsu*, R1017) were used. A combination of two glass filters NIR-blocking (*LINOS*, Calflex X) and long-pass (*SCHOTT*, RG590) were used to suppress background light. The filters were joined with each other and with the PMT viewport using optical grease. In order to reduce dark counts, the PMTs were cooled down to about -20 °C using a peltier-based housing. However no HFS-fluorescence signal was observed on these PMTs, which also explains the failing attempts to observe the fluorescence in previous beamtimes, when only this setup was available. Here, we used additionally a new, parabolic mirror, which turned out to be the suitable device for signal detection of lithium-like bismuth, confirming the simulations that were carried out previously [35].

3.5.3. Parabolic mirror Simulations of the distribution in the laboratory frame indicated that the fluorescence collection efficiency of the segmented mirror system, taking into account the wavelength dependence of the PMT quantum efficiency, is insufficient for the detection of the lithium-like bismuth fluorescence [35]. In a first beamtime in 2004 the PMT's were replaced by avalanche photodiodes in order to shift the sensitivity of the detectors into the red region. Unfortunately the combination

of electrical noise and long-lived fluorescence of collisionally excited molecular states of residual-gas atoms created a prohibitively large background floor with a high noise level.

Hence a new detection system was developed that is able to collect a large fraction of the photons emitted in the forward direction. A simplified schematic view is shown in figure 3 and it is described in detail in [35]. Hence, only a brief description will be given here: The system consists of a mirror mounted on a retractable linear feedthrough. The mirror has a diameter of 150 mm and the mirror's reflective surface follows the function $x^2/400$ mm, where x is the distance between the window and the mirror. It is made of copper since this material has a high reflectivity between 600 nm and 700 nm and is compatible with UHV conditions inside the storage ring. The mirror has a central cut to allow the ions to pass through but the fluorescence emitted at small angles to the forward direction is collected and directed towards the PMT. Therefore the detection probability for photons emitted at angles $\leq 25°$ with respect to the ion-beam direction that fall within the quantum efficiency of the PMT is dramatrically increased. An additional reflecting cone, as depicted in figure 3, is installed to further enhance the collection efficiency. The reflected fluorescence passes through a window, a light-guide and the same filter combination as described above: an NIR-blocking (*LINOS*, Calflex X) and a long-pass filter (*SCHOTT*, RG590), before it hits the photo cathode of the PMT. Also here the PMT is installed into a peltier-based housing. About 1 mm gap was kept between the surfaces of the window and the light-guide, then all the other surfaces were joined together using optical grease in order to avoid reflection losses. The aperture of the central cut was chosen to be at least 3σ of the typical radius of the electron-cooled ion-beam which was estimated to be about 10 mm FWHM. Since the ion beam might have considerably larger diameter after injection from SIS, the mirror is moved out of the beam with the linear feedthrough using a remotely controlled pneumatic drive. Once the beam is cooled, the mirror is moved in place in about 1 s. Typically a loss of less than 10% of the ion beam is observed during this process. Once the mirror was installed at the beamline, it was first centered around the design orbit using a He-Ne laser and two scrapers installed in this straight section of the beamline, which are located symmetrically with respect to the gas target.

3.6. Data Acquisition

Fast moving ions induce an isotropic fluorescence background by collisions with the residual-gas molecules inside the vacuum beamline [36]. This induced-background fluorescence covers the visible region and exhibits fast ultraviolet and blue as well as slower red and infrared components. This background will therefore produce signals on the PMT. This signal can be used for timing synchronization of the laser pulse with the ion bunch position and the determination of the bunch length as described in [32, 33] and section 3.7, however its noise level can bury the HFS-fluorescence signal. The central development in the new data acquisition system was the time-tagging for every detected photon. It considerably simplified the synchronization and timing of all time-critical

parameters and allowed for a post-beamtime optimization of the acceptance windows for fluorescence photons from the ion bunches. The ion bunches revolving inside the storage ring with a phase shift of 180° were created with a sinusoidal signal at twice the revolution frequency (~ 4 MHz) that was produced by a radio frequency generator amplified typically 500 V and up to 700 V and applied to one of the radio frequency cavities as shown in figure 2.

A part of the RF signal was discriminated, divided by a factor 200 to about 20 kHz and used as a common stop signal for a multihit multichannel time-to-digital converter (TDC) realized on a field programmable gate array (FPGA). Hence each photon has a timing information between 0 and 50 μs with a fixed phase relation to the bunching frequency. The only information required in the analysis is the arrival time of the photon within a single revolution. The FPGA has a time resolution of $10/3$ ns given by the 300 MHz clock. The temporal distance between two stop signals is then 50 μs, which corresponds to 100 ion revolutions.

The signals of 12 detectors were recorded by the TDC. Six of these detectors were dedicated to scan for the fluorescence signal. They were located at the mirror section (solar blind and three Hamamatsu R1017 for hydrogen-like and lithium-like ion, respectively), at the parabolic mirror system (Hamamatsu R1017) and at the forward detection system (*Hamamatsu*, R943-02). The latter was installed at the laser beamport in the forward direction on the target side as shown in the lower left side of figure 2, where we tried to observe a fluorescence signal directly in the forward direction. The signals of these photomultipliers were amplified by a 16 channel fast amplifier (*CAEN*, 979) before signal transfer to the DAQ-room and there fed to an inductive decoupling unit (*GSI*, AP2005) before being processed by a 16 channel constant fraction discriminator (*CAEN*, N843). Four additional detectors were mounted at various places in the ESR. Another photomultiplier was located at the gas-jet target, whereas two UV PMTs and a channeltron were located between the gas-jet target and the mirror section [33] (not shown in figure 2. The signals of these detectors were amplified and also passed to the inductive decoupling unit and the constant fraction discriminator. For accurate timing the signal travel times of all detectors were matched with delay units as needed before being translated for the TDC input by two NIM to ECL level adapters (*GSI*, EC 1601). In order to determine the moment of the entrance of the laser pulse into the ESR, fast photodiodes were placed near the laser entrance windows of the ESR. The signals of these diodes were also recorded using the TDC. Besides the various photon detectors the only other parameter recorded by the TDC was the Q-switch signal of the pumping laser.

3.7. Timing

Figure 4 shows the signal used to synchronize the ion bunches with the laser pulses. Due to the prompt UV response of the collision-induced background, the solar-blind PMT was used to establish the right timing of the laser pulse. Its signal is plotted as
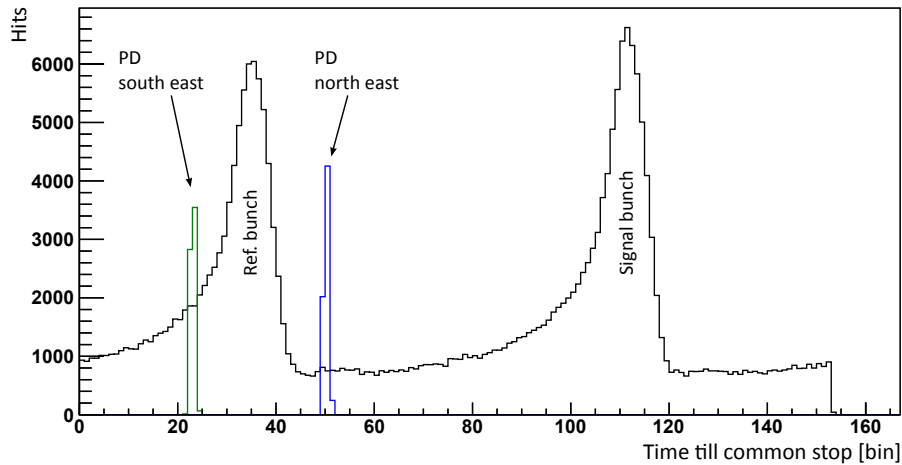
Figure 4. Profile of the bunch structure. The time delay applied to the pulsed laser is adjusted until the peaks of the photodiodes (PD) are located symmetrically around one of the ion bunch signals. Then one can be sure that the laser pulse hits only one of the bunches at the electron cooler section. Please note that the time on the x axis is inverted since the remaining time after the event until the common stop signal appeared is used. For more details see text.

a function of time till common stop modulo the revolution time. A full revolution of about 510 ns is divided in 153 bins, each corresponding to a 300 MHz TDC-timing unit equivalent to 10/3 ns. The bunch structure with two peaks is clearly visible: the maxima of the peaks appear in about bin 37 and 112. The peak width (FWHM) corresponds to a length of about 7 m in the laboratory frame.

To synchronize the laser pulse with the ion bunches, two fast pin-photodiodes (PD) were installed at the entrance and exit windows at the ESR as depicted in figure 2. They detect light scattered at the windows and the induced signals were then transported to the DAQ-system with cables of identical length and travel time adjusted to the PMT-signals. Here they are discriminated and fed into the multihit TDC. A histogram of these signals is also included in figure 4. The time gap between both PD-signals is fixed and given by the laser pulse travel time through the straight section of the ESR. The positions of these signals were then adjusted by changing the delay time of the trigger pulse applied to the pump laser's Pockels-cell until they appeared symmetrically with respect to the maximum of one of the bunches (the reference bunch). In this way it was ensured that the laser pulse coincides with the signal bunch in the electron-cooler section. Please note that on this plot the photodiode signals caused by the laser pulse appear to the left and the right of the reference bunch, because the photodiodes are located on the opposite side of the ring. Hence, the reference bunch is observed at the detection region while the signal bunch is being illuminated by the laser pulse at the electron-cooler section.

3.8. Experiment execution

Settings were first optimized to have the orbit of the cooled beam passing through the center of the retractable copper mirror. On the cooler side, the beam was optimized to pass through the center of the e^--beam to obtain optimal cooling and then the laser beam was superimposed with the ion beam using the scrapers.

The measurement cycle consisted of electron cooling after injection for about 30 s. Then the mirror was moved into the beam (only Bi^{80+}) and the laser scan was started. Typically after about 15 min the ion beam current went down to about 60-70% of the starting value. The mirror was removed and a new injection triggered.

The storage ring was first optimized for the storage of Bi^{82+} and the known resonance in the hydrogen-like ion recorded. Unfortunately, the statistics were much worse than in all previous beamtimes which was afterwards related to a bad transmission of the viewport. Then, the ring settings were optimized for Bi^{80+} and the laser switched to 640 nm and operated in broadband mode to simplify the search for the resonance. The resonance structure was soon observed and verified before the laser was switched to narrow-bandwidth operation. The resonance was recorded with sufficient statistics and systematic variations of the experimental parameters were carried out.

4. Data analysis

The data obtained was analyszed independently using two different approaches [38, 39]. Both resulted in consistent results for the central laser wavelengths. In the following the fitting procedure used in [39] is described in detail. A single scan for lithium-like bismuth was typically recorded in about 5 minutes. The scan range of 0.5 nm was divided into 51 steps ($\Delta\lambda = 0.01$ nm). For each step, the signal strength and the laser wavelength was extracted from the raw data using the following procedure: The data of a single TDC common stop period – corresponding to 100 ion revolutions since the common stop signal is obtained from the bunching frequency by a 1:200 rate divider – is binned with respect to the revolution phase to obtain the bunch structure as it is shown in figure 5. Count rate uncertainties are attributed according to Poisson statistics. These histograms are fitted by two Gaussians and a constant offset. The fit function is parametrized such that the difference ΔA of the areas of the Gaussians, which is the observed signal rate, is a fit parameter itself:

$$f(x) = y_0 + \frac{A_1}{\sqrt{2\pi}w_1} \exp\left[\frac{(x - t_1)^2}{2w_1{}^2}\right] + \frac{A_1 + \Delta A}{\sqrt{2\pi}w_2} \exp\left[\frac{(x - t_2)^2}{2w_2{}^2}\right] \qquad (6)$$

Thus, the area difference and the corresponding error are obtained directly from the fitted parameters without the need to perform an error propagation of correlated uncertainties. For each step the mean laser wavelength λ_{step} along with its uncertainty $\Delta\lambda$ as well as the mean laser intensity I_{laser} is calculated from all wavemeter data recorded during the corresponding time interval. The resonance structure is then obtained by plotting the area differences of the TDC data normalized to the ion current
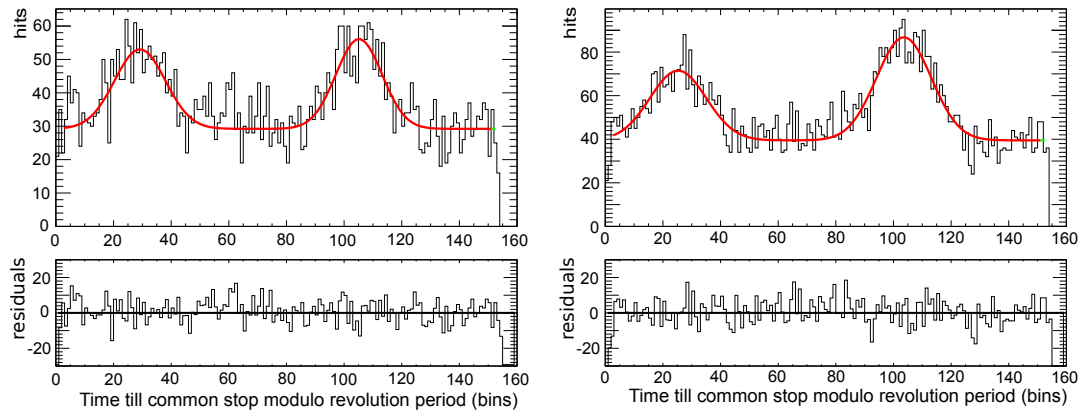
Figure 5. Two examples of the TDC histogram fits: the left one is taken with the laser slightly off resonance and therefore the peak of the reference bunch has approximately the same area as that of the signal bunch. The right one is on resonance and the area and amplitude of the signal bunch peak is clearly larger than that of the reference bunch. More details in text.

and the measuring time, as a function of the laser wavelength and performing a fit of a Gaussian resonance curve to the data. Since several scans were combined to a single spectrum, but the wavelength information of the individual scans is not identical, the combination was performed using different strategies: (1) To avoid binning problems, every data point is plotted with its individual wavelength. (2) Alternatively, a binned version of the data is produced by splitting the normalized count rate of each step multiplied with the actual ion current into two fractions depending on the relative position of the step's wavelength between two neighboring bins of the histogram. By also dividing the measuring time, multiplied also by the actual ion current, in the same fashion, the signal rates are again normalized to cps/mA. Figure 6 shows an example of the corresponding datasets and the fits; the central value of the Gaussian along with its uncertainty denotes the fitted transition wavelength λ_{fit} with the error $\Delta\lambda_{\text{fit}}$. The residuals are normalized to the uncertainty of the corresponding data point σ_i. The results of both strategies agree within their uncertainties and also with another independent analysis [39] using similar but slightly distinct approaches to bin the data. The fits yielded full-widths at half-maximum of $\approx 100\,\text{GHz}$ and statistically distributed fit residuals.

5. Results

5.1. Transition wavelength in the laboratory frame

All resonances of lithium-like and hydrogen-like bismuth that were taken during the beamtime with varying parameters have been analyzed using the procedure described in the previous section. While the uncertainties of the center wavelengths resulting from the fits only take into account the statistical uncertainty of the data of the individual runs, systematic uncertainties have to be evaluated additionally. This was performed
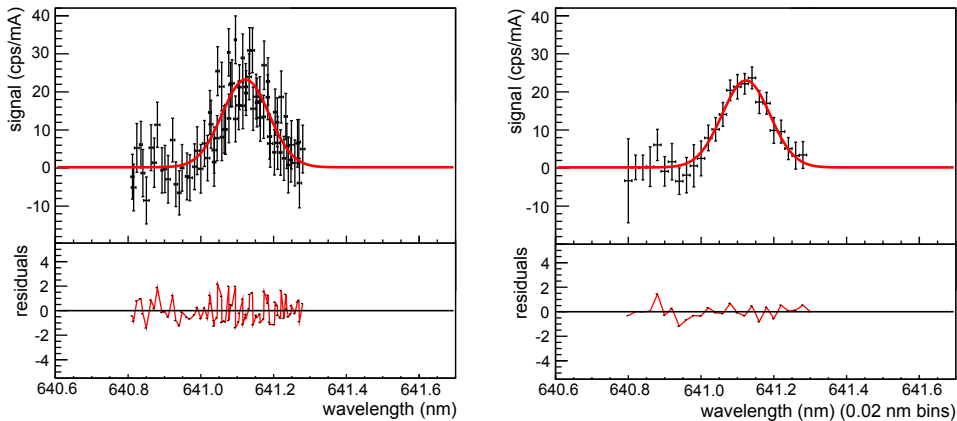
Figure 6. Examples of the resonance fit of a single spectrum. The left plot shows the fit of the unbinned data, while the right one is binned with a bin width of 0.01 nm.

by analyzing the data individually and searching for effects causing the variations of the resonance position. The results are as follows:

Ion beam current: Spectra were recorded for typical ion beam currents between 1.5 and 3.0 mA and some spectra were also recorded for 0.5 mA. All the values were obtained for an RF voltage amplitude of 500 V. The central wavelength was then plotted as a function of the ion beam current and the data were fitted with a linear function. No significant dependence of the central wavelength with respect to the ion beam current was observed, however the data scatter around the mean value by about 10 pm. In order to obtain a conservative upper limit for the uncertainty introduced by this effect, the value extrapolated at zero ion beam current was calculated and its uncertainty is obtained as $\Delta\lambda_{\mathrm{I-ion}} = 11.5$ pm in the laboratory frame.

RF Amplitude: Spectra were recorded for different RF-voltage amplitudes applied to the RF-cavity. As explained in section 3.1 this leads to bunched ion beams. Here all the parameters except the RF amplitude were kept constant. Spectra were then recorded for voltage amplitudes between 100 and 700 V in 200 V steps. Similar to the investigation of the ion-beam current dependence, the fitted central wavelength was calculated and plotted as a function of the RF amplitude. The data were then fitted with a linear function. In first approximation the central wavelength shows almost no dependence on the RF voltage amplitude. In order to get a conservative value of the systematic introduced by this effect, the maximum scatter around the standard value of $U_{\mathrm{RF}} = 500$ V was calculated. The obtained value is $\Delta\lambda_{\mathrm{RF}} = 6$ pm.

Angular deviation: As it was mentioned in section 3.3, the straight sections of the ESR are terminated with axial windows through which the laser beams can be coupled into the beamline. The windows are mounted on CF-63 flanges with a free aperture of $d = 60$ mm. However the windows are not necessarily centered with respect to the ion beam axis. Hence a He-Ne laser beam was aligned through the straight section of the beamline using a pair of scrapers at the electron cooler. The position

of the windows was then checked with respect to the position of the He-Ne laser beam. The uncertainty introduced by the possible misalignment between the laser and ion beam is then conservatively estimated from the maximum deviation the laser beam could have within the aperture of the windows. The free aperture of 60 mm and the separation between both windows of 23 m results in an angular uncertainty of $\Delta\theta_{\mathrm{max}} \approx 2.6$ mrad. This corresponds to a wavelength uncertainty of $\Delta\lambda_\theta = |\gamma\lambda_0\beta(\cos\Delta\theta_{\mathrm{max}} - 1)|$. For the case of collinear and anticollinear spectroscopy we obtain 5 pm and 0.8 pm, respectively, in the laboratory frame.

Wavelength calibration: The laser wavelength was not actively stabilized, but measured for each individual laser shot with a wavemeter. For each wavelength step, all measured values were averaged. When the laser was operated in broadband mode, only a single Fizeau interferometer could be used while for operation with the smaller bandwidth two interferometers were used. The wavemeter exhibits a relative accuracy of 10^{-7} if it is operated with all four interferometers. In order to estimate the relative accuracy when using only one or two interferometers, the wavelength of the reference helium-neon laser was measured after the beamtime using only the restricted number of interferometers and the deviation from the nominated wavelength was obtained. Additionally, the influence of the spectral asymmetry of the pulsed dye laser was estimated to introduce a systematic uncertainty of one quarter of the FWHM of the laser linewidth, which - in the narrow configuration - is given by 26 pm. The estimated total uncertainty of the wavelength calibration is therefore $\Delta\lambda_{\mathrm{cal}} = 17$ pm.
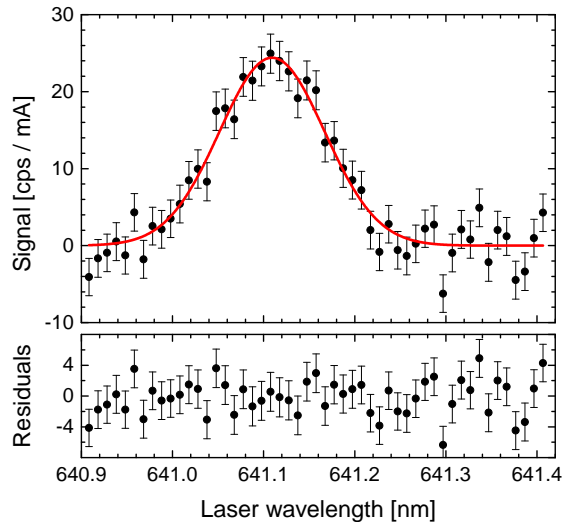
Figure 7. Resonance of the ground-state hyperfine structure transition in lithium-like Bi^{80+}. Normalized signal rate as a function of laser wavelength. The solid line is an error weighted Gaussian fit without background assumed.

5.2. Rest-frame transition wavelength

The crucial step in the analysis is the transformation from the laboratory frame into the ions' rest frame, requiring accurate information about the ion speed. In principle the ions should have adapted to the velocity of the electrons in the cooler section after sufficient cooling time [40]. The electron velocity can be determined from the electron cooler voltage using

$$\beta = \sqrt{1 - \gamma^{-2}} = \sqrt{1 - \left(1 + \frac{eU}{m_e c^2}\right)^{-2}}, \tag{7}$$

where $\beta = v/c$ is the velocity, e the elementary charge, U the electron accelerating potential difference, and m_e the electron mass. The measurements were performed at a nominal electron cooler voltage of $U_{\text{set}} = -213\,900$ V for $\text{Bi}^{82+}$and $-213\,890$ V for Bi^{80+}. To estimate the uncertainty of the ion velocity, the relation between the set-voltage and the applied voltage of the electron cooler high-voltage device has to be taken into account. Additional corrections for the space charge of the electron and the ion beam as well as their related uncertainties must be considered.

The space charge correction of the electron beam was experimentally determined by turning off the bunching frequency, grounding the RF-cavity and varying the ion cooler current from the usually applied 200 mA down to 10 mA. This electron current is still sufficient to keep the beam cold. During this process the increasing Schottky frequency of the circulating ion beam is observed and once the 10 mA current is reached the electron cooler voltage is decreased until the original revolution frequency is covered. Additional corrections for the space charge of the electron beam Φ_e and the ion beam according to

$$\Phi_e = \varphi \, \frac{I}{\beta} \tag{8}$$

as well as their related uncertainties must be considered. Here, φ is the proportionality factor for the space charge correction, I is the electron current and β the ion (and electron) velocity. The required change of voltage directly reflects the electron-beam space-charge correction and a correction factor of $\varphi_{\text{exp}} = 0.111$ V/mA is obtained. This is in excellent agreement with a theoretical estimation of $\varphi_{\text{theo}} = 0.112$ V/mA based on a cylindrically symmetric electron beam potential and the ion beam passing through the central potential. As discussed before, an influence of the ion beam current on the resonance wavelength was not observed and according to theoretical estimations it should be only a –4.2 V contribution which is added to the electron space charge of 31.4 V and assumed as the total space-charge correction uncertainty. The complete space charge correction therefore amounts to $\delta U_{\text{space-charge}} = 27(4)$ V.

The relation between the electron-cooler set-voltage and the real voltage applying at the cooler terminal was determined with a high-voltage voltmeter (*Heinzinger*, HVDVM 131) up to -100 kV, which is its maximum operating voltage. This voltmeter was calibrated in 2001 at the *Physikalisch Technische Bundesanstalt (PTB)* in Braunschweig. A voltmeter for -214 kV that could have recorded the voltage during the measurements

Table 4. Electron cooler settings used during the experiment as described in the text.

	Bi^{82+}	Bi^{80+}	Units
Electron current	200	150	mA
U_{set}	$-213\,900$	$-213\,890$	V
Calibration correction	$-132(85)$	$-132(85)$	V
Reproducibility e-cooler voltage	± 25	± 25	V
$U_{\text{e-cooler}}$	$-214\,030(110)$	$-214\,021(110)$	V
Space charge correction	$27(4)$	$19(4)$	V
Misaligned bunching frequency	-	$67(5)$	V
U_{eff}	$-214\,005(110)$	$-213\,935(110)$	V
Calculated ion velocity β	$0.709\,38(29)$	$0.709\,32(31)$	

was not available at that time. Instead, an extrapolation of the calibration relation from the range of $+20$ to $+100$ kV down to -214 kV became necessary. Additionally, a series of independent measurements that were taken between 2001 and the time of the measurement in 2011 pointed to a significant temporal change either of the GSI voltmeter calibration or of the electron cooler power supply during that period. This was also indicated by a recalibration at PTB in 2012 where a significant shift against the 2001 calibration was observed for positive voltages. A similar drift is expected for negative voltages but could not be verified anymore due to a breakdown of the voltmeter (*Heinzinger*, HVDVM 131). We have taken into account all available information and extrapolated the high-voltage calibrations with a second-order polynomial to account for the expected quadratic dependence of the heating power $P = U \cdot I = U^2/R$ on the voltage. Based on the observed drift of the positive branch and assuming, that the asymmetry between the positive and the negative branch was conserved, we have estimated the corresponding drift on negative voltages and obtained a total calibration correction of 131 V. Statistical and systematic uncertainties were treated independently and added in quadrature for the statistical uncertainties and linearly in the case of the systematic uncertainty, resulting in 20 V and 65 V, respectively. Finally we observed in a few test experiments as well as during a laser-cooling beamtime at the ESR [31] an occasional voltage shift of about 25 V after resetting the cooler voltage power supply. This reproducibility is taken into account as an additional uncertainty of 25 V, which is also added linearly to the systematic uncertainty. All contributions and the final value for the effective electron acceleration voltage and its uncertainty, are listed in table 4.

In the case of lithium-like bismuth there was an additional complication: Usually the free revolution frequency of the ions is measured in the coasting beam mode, i.e. without applying an RF voltage at the bunching cavity. Then, twice this frequency $f_{\text{RF}} = 2 \cdot f_{\text{rev}}$ is applied to the RF cavity to ensure that the RF bucket force and the electron-cooler force have the zero-crossing at the same ion speed and are therefore driving the ions to the same velocity. For unknown reasons it turned out at the end of the beamtime that the two were not ideally matched. Since the average force of the RF bucket during one revolution is stronger than the cooling force of the electron cooler,

Table 5. Wavelengths and transition energies of the HFS-transitions in highly charged ^{209}Bi and the specific difference $\Delta' E$ according to (2). All values were obtained using ion speed determination from the electron cooler voltage with all corrections and uncertainties as described in the text.

	[nm]	[meV]	Reference
Bi^{82+}	243.75(2)(5)	5086.3(03)(11)	This work
Bi^{80+}	1554.66(10)(33)	797.50(05)(17)	This work
$\Delta' E$	-	$-61.37(08)(35)$	This work
$\Delta' E$ (Theory)	-	$-61.320(6)$	[22]

we have determined the effective mismatch as a voltage difference between the electron cooler set-point and the real ion beam velocity, which was found to be 67(5) V. This is also included in table 4.

The rest frame HFS-transition wavelengths are then calculated using the relativistic Doppler formula $\lambda_0 = \lambda_{\text{lab}} \cdot \gamma (1 \mp \beta)$ and (7) for Bi^{82+} and Bi^{80+}. The values and uncertainties are summarized in table 5. Our value for the HFS in Bi^{82+} resulting from this analysis and presented before in [17] is two orders of magnitude more precise than the only experimental value reported previously, determined indirectly via x-ray emission spectroscopy [16].
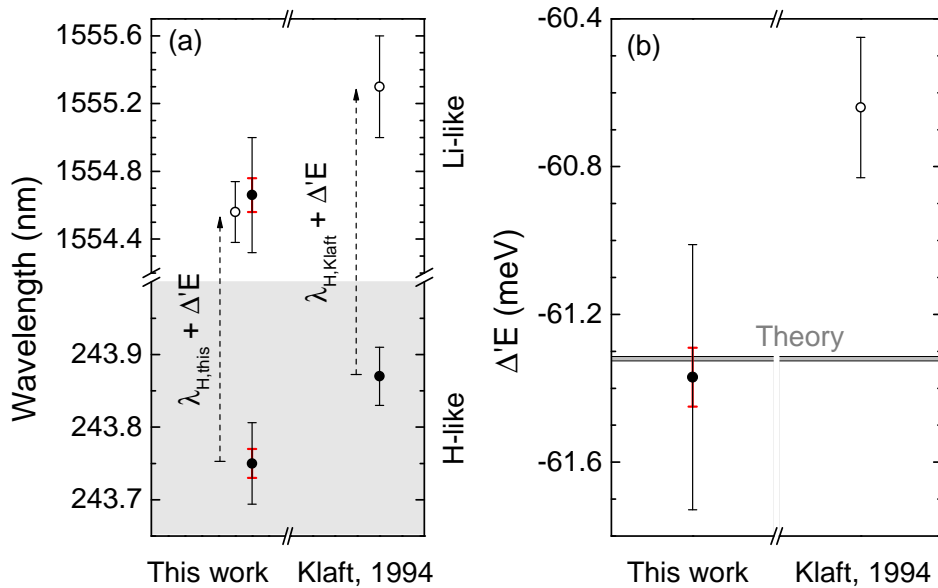

Figure 8. (a) Wavelengths of the transitions in hydrogen-like and lithium-like bismuth. More details see text. (b) Specific difference $\Delta' E$ of the hyperfine splitting. Experimental results are shown as filled circles. In this work the red and black error bars indicate the statistical and total uncertainties, respectively. The open circle represents the case where it is assumed that the value from Klaft *et al* [10] for the hydrogen-like bismuth is correct and our voltage calibration was adapted to reproduce this value as discussed in section 5.3, see (9) and following text.

The left part of figure. 8(a) shows the wavelength of both transitions obtained in this work with their statistical and systematic uncertainties and compares them with the result from Klaft et al. [10] for the hydrogen-like ion and the prediction for the lithium-like ion based on the combination of the value of Klaft *et al* and the specific difference calculated in [22]. Our value for the hydrogen-like ion is considerably different from the previous one but the error bars representing the systematic uncertainties do almost overlap. The error bars of the lithium-like result and the prediction do overlap, but one has to keep in mind that the latter is based on a different value for the hydrogen-like transition wavelength. Starting with the hydrogen-like value observed here and using the $\Delta' E$ value from [22], one obtains a prediction of $\Delta E_{\mathrm{HFS}} = 797.55(9)\,\mathrm{meV}$, corresponding to $\lambda = 1554.56(18)\,\mathrm{nm}$ for the lithium-like transition. The correlated uncertainty of the voltage calibration is neglected here, since both our measurements were made using the same calibration. However, the contribution of $25\,\mathrm{V}$ corresponding to the electron cooler reproducibility (which is about 22% of the total systematic uncertainty) and the statistical uncertainty have been taken into account. The prediction is in very good agreement with our experimental value.

5.3. Specific difference $\Delta' E$

In the last two rows of table 5 the specific difference $\Delta' E$ is given as calculated from our experimental transition wavelengths and compared to the predicted value from theory. They are in excellent agreement, even within the statistical uncertainty, as can also be seen in the left part of figure 8(b). In figure 9 the individual contributions to $\Delta' E$ which are free of experimental input are shown as listed in table 3 and the arrows represent the experimental sensitivity to the contributions according to the statistical and the systematic uncertainty. Our result confirms the dominating contributions in the specific difference, the Dirac term, and the interelectronic-interaction corrections, on a 5×10^{-3} level. The latter – being up to 70% of relativistic origin – can only be evaluated within a rigorous QED approach. Thus, we have effectively tested the relativistic interelectronic-interaction in the presence of a strong magnetic field in a heavy highly charged ion for the first time. According to the individual contributions listed in table 3, we have tested the specific difference in the Dirac values and the first order $(1/Z)$ of the interelectronic interaction with an accuracy at the 1% level. To achieve the required accuracy in these calculations, theory has to go beyond the Coulomb approximation and needs to include the Breit interaction. The Breit term accounts for magnetic interactions and retardation effects to the order of $1/c^2$ and represents about 2.2% of the total value of $\Delta' E$ [42] – its importance has been unambiguously confirmed by our result. A measurement with similar statistical uncertainty but a better control on the voltage systematic will allow for a first test of the screened QED contributions. Such a measurement has been performed in the meantime at the ESR using a 200-kV high-voltage divider and further improvements in data acquisition, but analysis of this data is still ongoing. First results have already been presented in [32] and results of a partial analysis of a subsection of
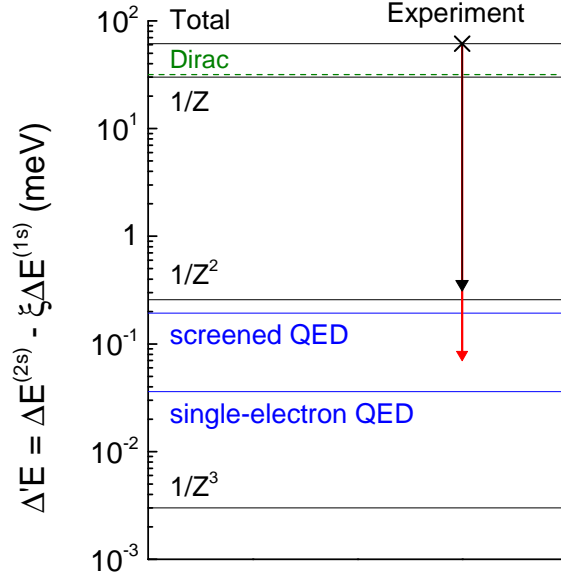
Figure 9. Individual contributions to $\Delta'E$ according to table 3. The uppermost line represents the total value, the dotted line is the contribution from the specific difference of the Dirac values for the hydrogen-like and the lithium-like ion, while the other lines represent the contributions of the electron-electron interaction which is expanded in powers of $1/Z$. The two blue lines indicate the QED contribution from the screened QED and from the single-electron QED. The experimental sensitivities are given by the red and black arrows, which represent the statistical and systematic uncertainties, respectively. Only the systematic uncertainty caused by the high-voltage measurement prevents a test of the screened QED.

hydrogen-like data is in reasonable agreement with the result of the experiment reported here. QED on the single-electron level does unfortunately largely cancel in $\Delta'E$ and a reasonable test of this contribution requires further reduction of the uncertainty in both transitions by at least one order of magnitude. This improvement cannot be achieved at a storage ring. Therefore the SpecTrap Penning trap is currently being installed at the HITRAP facility [41] at the GSI Helmholtz Centre for Heavy Ion Research that is especially designed for laser spectroscopy on the ground state of hydrogen-like and lithium-like heavy ions [43, 44].

Finally, we like addressing the consequence of the discrepancy between the transition wavelength in the hydrogenlike ions for the specific difference. One might argue that the value reported by Klaft and coworkers [10] might be less affected by the high-voltage issue since (i) the measurement was performed much closer in time to the calibration of the voltmeter (*Heinzinger*, HVDVM 131) at the PTB and (ii) a much lower high-voltage of only 120 kV was used which does not require such a far extrapolation as in our case. Hence, we have performed an additional analysis assuming that the 1994 measurement was correct and our discrepancy is based on a miscalibration even larger than anticipated by our estimated systematic uncertainty. We further presume that the

miscalibration affects both our measurements in the same way. Since the hydrogenlike
and the lithiumlike measurements are performed at almost equal velocity, we can write

$$\lambda_{\text{lab}}^{(82+)} \cdot \lambda_{\text{lab}}^{(80+)} = \lambda_0^{(82+)} \gamma \left(1 + \beta\right) \cdot \lambda_0^{(80+)} \gamma \left(1 - \beta\right) \quad = \lambda_0^{(82+)} \cdot \lambda_0^{(80+)} \quad (9)$$

where we have neglected the tiny difference of $\delta\beta \approx 7 \cdot 10^{-5}$ between the two
measurements. Solving this equation for the rest-frame transition wavelength of the
lithium-like ion $\lambda_0^{(80+)}$ and using the value from Klaft and coworkers for $\lambda_0^{(82+)}$ as well
as our laboratory wavelengths for both species, we obtain

$$\lambda_0^{(80+)} = \frac{\lambda_{\text{lab}}^{(82+)} \cdot \lambda_{\text{lab}}^{(80+)}}{\lambda_0^{(82+)}} = 1554.16(27)\,\text{nm}, \quad (10)$$

which does not agree with the predicted wavelength.

Performing a full calculation by using the Klaft et al. value to recalibrate the cooler
during the 2011 measurements and using this calibration also for the lithium-like case,
we obtain $\lambda_0^{(80+)} = 1553.96(29)\,\text{nm}$, which is only slightly different and does also not
agree with the predicted wavelength. Accordingly, it is not surprising that the value
for $\Delta'E = -60.62(20)$ based on these recalibrated values is also considerably off from
theory as shown in figure 8(b).

As a summary, we have to state that the measurement of the transition wavelength
of the ground state hyperfine M1 transition in hydrogen-like and lithium-like bismuth
reported here confirms the predicted specific difference $\Delta'E$ at a 6×10^{-3} level. It
is, however, inconsistent with the result of the previous measurement of the transition
wavelength in Bi^{82+} from 1994 by Klaft and coworkers [10] at a 2σ level. The uncertainty
of all wavelengths and, consequently, of $\Delta'E$ is dominated by the correlated voltage
calibration uncertainty. The measurements of the transition wavelength in hydrogen-
like bismuth can be harmonized by adapting the voltage calibration but only at the
expense of losing the agreement with theory. This can only be resolved by a further
measurement with smaller uncertainties. Possible routes to such determinations are
experiments with an improved velocity determination of the ions inside the storage ring
as performed in 2014 at the ESR [32] or by performing the measurements on cooled
trapped ions. Both routes are being followed with experiments at GSI.

Acknowledgment

acknowledged. We thank the accelerator and storage ring divisions at GSI for their kind support during the beamtime and S. Minami and N. Kurz at the GSI experiment electronics department for their support in the data acquisition and the VUPROM development.

References

[1] Hanneke D, Fogwell S and Gabrielse G 2008 *Phys. Rev. Lett.* **100** 120801.
[2] Hagley E W and Pipkin F M 1994 *Phys. Rev. Lett.* **72** 1172.
[3] Sturm S, Wagner A, Schabinger B, Zatorski J, Harman Z, Quint W, Werth G, Keitel C H and Blaum K 2011 *Phys. Rev. Lett.* **107** 023002.
[4] Köhler F *et al* 2016 *Nat. Commun.* **7** 10246.
[5] Gumberidze A *et al* 2005 *Phys. Rev. Lett.* **94** 233001.
[6] Beiersdorfer P 2010 *J. Phys. B: At. Mol. Opt. Phys.* **43** 074032.
[7] Pohl R 2010 *Nature* **466** 213.
[8] Antognini A *et al* 2013 *Science* **339** 417.
[9] Werth G 2006 *Hyperfine Interac.* **172** 125.
[10] Klaft I *et al* 1994 *Phys. Rev. Lett.* **73** 2425.
[11] Seelig P *et al* 1998 *Phys. Rev. Lett.* **81** 4824.
[12] Crespo López-Urrutia J R, Beiersdorfer P, Savin D W and Widmann K 1996 *Phys. Rev. Lett.* **77** 826.
[13] Crespo López-Urrutia J R, Beiersdorfer P, Widmann K, Birkett B B, Mårtensson-Pendrill A-M and Gustavsson M G H 1998 *Phys. Rev. A* **57** 879.
[14] Beiersdorfer P *et al* 2001 *Phys. Rev. A* **64** 032506.
[15] Shabaev V M, Artemyev A N, Yerokhin V A, Zherebtsov O M and Soff G 2001 *Phys. Rev. Lett.* **86** 3959.
[16] Beiersdorfer, Osterheld P A L , Scofield J H, Crespo López-Urrutia J R and Widmann K 1998 *Phys. Rev. Lett.* **80** 3022.
[17] Lochmann M *et al* 2014 *Phys. Rev. A* **90** 030501.
[18] Beier T 2000 *Phys. Rep.* **339** 79.
[19] Boucard S and Indelicato P 2000 *Eur. Phys. J. D* **8** 59.
[20] Tomaselli M, Kühl T, Nörtershäuser W, Borneis S, Dax A, Marx D, Wang H and Fritzsche S 2002 *Phys. Rev. A* **65** 022502.
[21] Shabaev V M, Shabaeva M B, Tupitsyn I I, Yerokhin V A, Artemyev A N, Kühl T, Tomaselli M and Zherebtsov O M 1998 *Phys. Rev. A* **57** 149.
[22] Volotka A V, Glazov D A, Andreev O V, Shabaev V M, Tupitsyn I I and Plunien G 2012 *Phys. Rev. Lett.* **108** 073001.
[23] Shabaev V M, Shabaeva M B, Tupitsyn I I, Yerokhin V A, Artemyev A N, Kühl T, Tomaselli M and Zherebtsov O M 1998 *Phys. Rev. A* **58** 1610 Errata.
[24] Tomaselli M, Fritzsche S, Kühl T and Winter H 2000 *Hyperfine Interact* **127** 315.
[25] Shabaev V M, Artemyeva A N, Zherebtsov O M, Yerokhin V A, Plunien G and Soff G 2000 *Hyperfine Interact.* **127** 279.
[26] Sapirstein J and Cheng K T *Phys. Rev. A* **63** 032506.
[27] Franzke B 1987 *Nucl. Instrum. Meth. B* **24-25** 18.
[28] Brown I G 1994 *Rev. Sci. Instrum* **65** 3061.
[29] Nolden F *et al* 2011 *Nucl. Instrum. Meth. A* **659** 69.
[30] Steck M, Beller P, Beckert K, Franzke B and Nolden F 2004 *Nucl. Instrum. Meth. A* **532** 357.
[31] Winters D *et al* 2015 *Phys. Scr.* **T166** 014048.
[32] Ullmann J *et al* 2015 *J. Phys. B: At. Mol. Opt. Phys.* **48** 144022.
[33] Wen W *et al* 2013 *Nucl. Instrum. Meth A* **711** 90.

[34] Vollbrecht J *et al* 2015 *J. Phys. Conf. Ser.* **583** 012002.

[35] Hannen V *et al* 2013 *J. Instrum.* **8** 09018.

[36] Weber G *et al* 2009 *Phys. Rev. ST Accel. Beams* **12** 084201.

[37] Andreev O V, Glazov D A, Volotka A V, Shabaev V M and Plunien G 2012 *Phys. Rev. A* **85** 022510.

[38] Lochmann M 2013 PhD Thesis, Johannes Gutenberg-Universität, Mainz.

[39] Jöhren R 2013 PhD Thesis, Westfälischen Wilhelms-Universität, Münster.

[40] Poth H 1990 *Phys. Rep.* **196** 135 .

[41] Kluge H-J *et al* 2008 *Adv. Quantum Chem.* *53* **83**.

[42] Volotka A V 2016 (private communication).

[43] Andelkovic Z, Cazan R, Nörtershäuser W, Bharadia S, Segal D M, Thompson R C, Jöhren R, Vollbrecht J, Hannen J and Vogel M 2013 *Phys. Rev A* **87** 033423.

[44] Andelkovic Z *et al* 2015 *Hyperfine Interact.* **235** 37.